Revision 2

High-pressure Raman spectroscopy, vibrational mode calculation and heat capacity calculation of calcium ferrite-type $MgAl_2O_4$ and $CaAl_2O_4$

Hiroshi Kojitani[1*], Daniel M. Többens[2§], Masaki Akaogi[1]

[1] Dept. of Chemistry, Faculty of Science, Gakushuin University
1-5-1 Mejiro, Toshima-ku, Tokyo 171-8588, Japan

[2] Institution of Mineralogy and Petrography, University of Innsbruck
Innrain 52, Bruno-Sander-Haus, A-6020 Innsbruck, Austria

*E-mail: hiroshi.kojitani@gakushuin.ac.jp

[§] Present address:
Helmholtz-Zentrum Berlin für Materialien und Energie
Hahn-Meitner-Platz 1, D-14109 Berlin, Germany

Abstract

High-pressure micro-Raman spectroscopic measurements of calcium ferrite-type $MgAl_2O_4$ and $CaAl_2O_4$ were made using a diamond anvil cell high-pressure apparatus. The pressure dependence of frequencies of 18 Raman peaks for calcium ferrite-type $MgAl_2O_4$ and 26 Raman peaks for calcium ferrite-type $CaAl_2O_4$ were determined up to 20 GPa at ambient temperature. The mode Grüneisen parameter for each observed Raman mode was obtained from the pressure dependence of frequencies. Vibrational mode calculations by first principles using density functional theory were also performed for assignment of Raman peaks and for estimating frequencies of Raman inactive modes. From the obtained mode Grüneisen parameters and the results of the vibrational mode calculations, thermal Grüneisen parameters were determined to be 1.50(5) for calcium ferrite-type $MgAl_2O_4$ and 1.31(3) for calcium ferrite-type $CaAl_2O_4$. These thermal Grüneisen parameters were applied to heat capacity and vibrational entropy calculations using Kieffer model.

Keywords: Raman spectroscopy, high-pressure, Grüneisen parameter, heat capacity, calcium ferrite, $MgAl_2O_4$, $CaAl_2O_4$.

Introduction

Calcium ferrite is accepted as one of the high-pressure constituent minerals of mid-ocean ridge basalt at pressures higher than about 25 GPa (Irifune and Ringwood 1993; Kesson et al. 1994; Hirose et al. 1999; Funamori et al. 2000; Ono et al. 2001; Ricolleau et al. 2008). It is expected that the calcium ferrite phase may exist in the Earth's lower mantle, considering the subducted oceanic crust into the deep mantle. According to Guignot and Andrault (2004), calcium ferrite-type $MgAl_2O_4$, which is represented as $MgAl_2O_4$ CF hereafter, is the second most common endmember, following $NaAlSiO_4$ CF in the calcium ferrite phase system. It is important to clarify the phase stability of $MgAl_2O_4$ CF for better understanding of behaviors of the subducted basaltic crust. $CaAl_2O_4$ CF is less common endmember, compared with $NaAlSiO_4$, Mg_2SiO_4, and $MgFe_2O_4$ (Guignot and Andrault 2004), but it differs from $MgAl_2O_4$ CF only in the type of the divalent cations. Moreover, $CaAl_2O_4$ CF exhibits stability pressure which is lower than that of $MgAl_2O_4$ CF (Akaogi et al. 1999). Thus the crystal-chemical resemblance between $MgAl_2O_4$ CF and $CaAl_2O_4$ CF facilitates the comparison of the lattice vibrational features and their effect on the elastic and thermodynamic properties.

To thermodynamically discuss the stability fields of $MgAl_2O_4$ CF and $CaAl_2O_4$ CF, thermochemical data are needed. However, the available data of enthalpy, entropy, and heat capacity are still limited because of insufficient amounts of high-pressure synthetic samples for calorimetry and their instability at high temperature and ambient pressure. Information of lattice vibration is very useful to estimate entropy and heat capacity of these materials. Kojitani et al. (2003) calculated the heat capacities and the entropies of $MgAl_2O_4$ CF and $CaAl_2O_4$ CF using the

vibrational density of states (VDoS) models based on measured Raman spectra. In that study, only the observed Raman peaks were considered to construct the VDoS models without peak assignments. In addition, their thermal expansivities were assumed to be identical with that of $CaFe_2O_4$ in the calculation of the anharmonic effect on the heat capacities. These procedures resulted in large uncertainties of the calculated heat capacities, particularly at high temperature.

An isobaric heat capacity (C_P) results from the addition of an anharmonic effect to an isochoric heat capacity (C_V) by harmonic vibration. The thermal Grüneisen parameter (γ_{th}) is an important value, revealing the degree of anharmonicity. If an accurate γ_{th} is known, it is possible to evaluate more reliable anharmonic effect, especially at high temperature. However, γ_{th} is generally difficult to measure directly. To constrain the thermal Grüneisen parameter, mode Grüneisen parameters are very useful, which can be defined as

$$\gamma_i = -\frac{\partial \ln v_i}{\partial \ln V} \quad (1)$$

where v_i and V are the frequency of lattice vibrational mode i and volume, respectively. In this study, high-pressure Raman spectroscopic measurements of $MgAl_2O_4$ CF and $CaAl_2O_4$ CF were performed to determine the mode Grüneisen parameters from the pressure dependencies of their Raman shifts. Also, lattice vibrational mode calculations from first principles were used for assigning observed Raman peaks and for estimating vibrational frequencies of Raman inactive modes. The obtained mode Grüneisen parameters have been used to determine thermal Grüneisen parameters. The VDoS models, and the thermal Grüneisen parameters of $MgAl_2O_4$ CF and $CaAl_2O_4$ CF have been applied to calculate their heat capacities and vibrational entropies using the Kieffer's

model (Kieffer 1979a, 1979b).

Experimental methods

Sample syntheses

Samples for Raman spectroscopy were synthesized using a Kawai-type high-pressure apparatus at Gakushuin University. Details regarding the high-pressure technique are presented in earlier studies, e.g., Suzuki and Akaogi (1995) and Kubo and Akaogi (2000). $MgAl_2O_4$ CF was prepared by heating the starting sample of synthetic $MgAl_2O_4$ spinel at 27 GPa and 2373 K for 1 hour, and then, quenching and decompressing to ambient conditions. The recovered sample was crushed using a die made of tungsten carbide just after cooling using liquid nitrogen. This was the identical sample that was used for Rietveld refinement in the study by Kojitani et al. (2007). For the $CaAl_2O_4$ CF sample, the starting compound of $CaAl_2O_4$ with stuffed tridymite structure was kept at 15 GPa and 1873 K for 1 hour. Details of the preparation are presented in the study by Kojitani et al. (2003).

High-pressure Raman spectroscopy

Micro-Raman spectroscopy was performed using JASCO NRS-3100 at Gakushuin University.

An Nd:YAG laser with the wave length of 532.38 nm was irradiated to the samples. The laser beam diameter was 1–2 μm. Rayleigh scattering light was cut by a long wave path edge filter (Semrock RazorEdge LP03-532RE-25). Raman spectra were detected by a CCD detector. The data were collected by repeating an exposure of 50 s five times for $MgAl_2O_4$ and an exposure of 50 s three times for $CaAl_2O_4$. The wavenumbers of the Raman shifts were calibrated using those of trichloroethylene. The observed data were analyzed using PeakFit software (SPSS Inc.) for profile fitting.

Compression of the samples was made by a diamond anvil cell high-pressure apparatus (SINTEK MA4824C) at ambient temperature. The cullet size of the diamond anvils was 0.6 mm. Gasket was a sheet of SUS304 steel with 0.25-mm thickness. The sample chamber size was 0.2 mm in diameter. The pressure medium was a mixture of methanol:ethanol = 4:1 (volume ratio). The hydrostaticity of this pressure medium is ensured up to 9.8 GPa (Angel et al. 2007). Therefore, data measured between 10 and 20 GPa were collected under nonhydrostatic conditions. Run pressures were determined by the ruby R_1 line using Piermarini et al.'s (1975) equation.

Vibrational mode calculation

The calculations were done from first principles using 3D periodic density functional theory with Gaussian basis sets. The program CRYSTAL 09 (Dovesi et al. 2005) was employed for this purpose. The vibrational frequencies were calculated in harmonic approximation at Γ-point from

numerically computed second derivatives of the energy at a stationary point on the potential energy surface (Pascale et al. 2004), using a fully relaxed structure.

A Pack-Monkhorst k net with 8×8×8 points in the Brillouin zone was used. The level of numerical accuracy was increased over the default settings of the software, as described in the study by Többens and Kahlenberg (2011). The atom displacements used for the calculation of the force constant matrix were increased to a value of 0.002 au for $MgAl_2O_4$.

For the Hamiltonian, a variation of the PBE0 functional (Adamo and Barone 1999) was used. The Hartree-Fock contribution to the hybrid HF/DFT exchange correlation term was changed from the original 1/4 to a value of 1/6, which is the correct value for aluminates and similar compounds (Többens and Kahlenberg 2011), and it worked very well for $MgAl_2O_4$ and $CaAl_2O_4$.

In the calculation for $MgAl_2O_4$ CF, the basis sets of the atoms were selected as follows: For magnesium, an 8-511G(1) contraction based on the 8-511G contraction given in the study by McCarthy and Harrison (1994) was used; for aluminum, an 88-311G(11) contraction based on the unpublished 88-311G contraction by N. M. Harrison (1993) was used; and for oxygen, an 8-411G(11) contraction based on the 8-411G contraction given in the study by Towler et al. (1994) was used. For all basis sets, the exponents of the two most diffuse sp shells and those of the d shells were optimized to the following values: sp(Mg) = 0.610, 0.279; d(Mg) = 0.570; sp(Al) = 0.461, 0.209; d(Al) = 2.60, 0.50; sp(O) = 0.464, 0.179; and d(O) = 0.67, 0.22. In the calculation for $CaAl_2O_4$ CF, the basis sets of aluminum and oxygen were the same as those of $MgAl_2O_4$ CF. For calcium, an 86-511G(21) contraction based on the 86-511G(3) contraction given in the study by

158 Catti et al. (1991) was used. For all the basis sets, the exponents of the two most diffuse sp shells
159 and those of the d shells were optimized to the following values: sp(Al) = 0.461, 0.209; d(Al) =
160 2.35, 0.52; sp(O) = 0.464, 0.179; d(O) = 1.67, 0.40; sp(Ca) = 0.444, 0.264; and d(Ca) = 0.301. The
161 sp exponents of Al and O could be retained from the optimization in $MgAl_2O_4$ CF.
162
163
164 Results and discussion
165
166 Raman spectra observed at 1 atm
167
168 Raman peak positions for both $MgAl_2O_4$ CF and $CaAl_2O_4$ CF observed at ambient conditions
169 are shown in Table 1. The irreducible representation of the vibrational mode symmetry with space
170 group *Pbnm* is as follows:
171 $$\Gamma = 14A_g + 14B_{1g} + 7B_{2g} + 7B_{3g} + 7A_u + 7B_{1u} + 14B_{2u} + 14B_{3u}.$$
172 As the Raman active modes are $14A_g + 14B_{1g} + 7B_{2g} + 7B_{3g}$, the total 42 Raman active vibrational
173 modes are expected. In this study, 24 Raman peaks were observed for $MgAl_2O_4$ CF in the Raman
174 shift range of 100–1200 cm^{-1}. All of them were noted to be the same within the uncertainties as
175 those of Kojitani et al. (2003), although some of the peaks reported by Kojitani et al. (2003) were
176 not detected in this study.
177 We observed 29 Raman peaks for $CaAl_2O_4$ CF in the Raman shift range of 150–1100 cm^{-1}. All

178 the peak positions are very consistent with those represented by Kojitani et al. (2003). Several peaks
179 reported by Kojitani et al. (2003) were not observed in this study. On the other hand, the peak at 306
180 cm^{-1} was not recognized in the previous work (Kojitani et al. 2003).

181

182 Vibrational mode calculation

183

184 The calculated lattice parameters and atomic positions for $MgAl_2O_4$ CF and $CaAl_2O_4$ CF using
185 the density functional theory (DFT) calculation are tabulated in Table 2, compared with those
186 experimentally determined ones. In $MgAl_2O_4$ CF, all the calculated lattice parameters of the fully
187 relaxed structure were about 0.3% greater than those observed by Kojitani et al. (2007); for the unit
188 cell volume, the deviation was 0.8%. Also, the DFT calculation well reproduced the observed
189 atomic positions with deviations of a maximum of 0.8%. In $CaAl_2O_4$ CF, the calculated lattice
190 parameters were slightly greater than those measured by Lazic et al. (2006). However, the
191 deviations were smaller than 0.4%. The calculated atomic positions showed good agreement with
192 the observed ones within the deviations of 0.3%, except for the *y* coordinate of the O2 site
193 (deviation of 0.95%). This good agreement of the structures for both $MgAl_2O_4$ CF and $CaAl_2O_4$ CF
194 is a precondition for the calculation of reliable lattice vibrational mode frequencies.

195 The results of the vibrational mode calculation for $MgAl_2O_4$ CF are shown in Table 3. The
196 agreement of the calculated Raman frequencies with the observed ones was very good, with
197 maximum deviations of ±10 cm^{-1} and a standard deviation of 4.5 cm^{-1}. This is in concordance with

198 the expected accuracy for these calculations demonstrated in the study by Többens and Kahlenberg
199 (2011). A full assignment of the spectrum, limited only by the experimental resolution, could be
200 achieved. The results of the calculation suggest that there is no fundamental lattice vibration with a
201 frequency higher than about 900 cm^{-1}. Therefore, the Raman band observed at 1106 cm^{-1} is
202 probably explained by the overtone of the B_{1g} mode at 566 cm^{-1} or the combination tone of the A_g
203 mode at 528 cm^{-1} and the B_{1g} mode at 566 cm^{-1}. The mode analysis also suggests that several
204 observed Raman bands can be assigned to two or three vibrational modes. Except for these
205 overlapped modes, undetectable Raman active modes for $MgAl_2O_4$ CF in this study were found to
206 be B_{1g} at 267 cm^{-1}, B_{2g} at 311 cm^{-1}, A_g at 481 cm^{-1}, and B_{1g} at 514 cm^{-1}, where the frequencies are
207 obtained by calculation.

208 In Table 4, the results of vibrational mode calculation for $CaAl_2O_4$ CF are shown. The
209 agreement of the calculated Raman frequencies with the observed ones was even better than that in
210 the case of $MgAl_2O_4$ CF, with maximum deviations of ±7 cm^{-1} and a standard deviation of 3.0 cm^{-1}.
211 This suggests that a full assignment of the spectrum could be achieved. The results of the
212 calculation suggest that the fundamental lattice vibrations have frequencies lower than 800 cm^{-1}.
213 Therefore, the two Raman bands observed at 925 and 1086 cm^{-1} are probably assigned to the
214 overtones of the B_{2g} mode at 459 cm^{-1} and the B_{1g} or B_{2g} mode at 543 cm^{-1}, respectively. By
215 considering the several overlapped modes, four Raman active modes for $CaAl_2O_4$ CF, B_{1g} at 265
216 cm^{-1}, B_{1g} at 365 cm^{-1}, B_{3g} at 536 cm^{-1}, and B_{1g} at 628 cm^{-1}, could not be observed in this study.

217 In both $MgAl_2O_4$ CF and $CaAl_2O_4$ CF, the vibrational modes with frequencies lower than about

300 cm^{-1} were found to mainly contain translation of the divalent cation (Mg^{2+} or Ca^{2+}). In the frequency range of 300–400 cm^{-1}, the translation of Al^{3+} was found to be the main vibration in most of the modes. At frequencies higher than about 400 cm^{-1}, the main types of the lattice vibrations are deformations of AlO_6 octahedra, instead of the translations of cations. Kojitani et al. (2003) implied that both the most intense Raman peaks of $CaAl_2O_4$ CF (at 704 cm^{-1}) and $MgAl_2O_4$ CF (at 708 cm^{-1}) are caused by vibrational modes related to only AlO_6 octahedra, because they might be independent of the difference in the divalent cations between Mg^{2+} and Ca^{2+}, as inferred from their very close frequencies. It should be noticed that the calculation results propose the same vibrational mode of A_g and B_{1g} with only deformation of AlO_6 octahedra for both the most intense Raman peaks of $MgAl_2O_4$ CF and $CaAl_2O_4$ CF.

High-pressure Raman spectra

Typical Raman spectra of $CaAl_2O_4$ CF observed at high pressures and ambient pressure are shown in Fig. 1. The Raman peaks observed at 15.6 and 17.8 GPa are broader than those of 1 atm, 6.2 GPa, and 9.3 GPa, which is probably due to the deviation from hydrostatic conditions above 9.8 GPa. As the relative intensities of the peaks in the range of 250–400 cm^{-1} are weak, precise determination of peak positions was not easy in this Raman shift range. It can be noted from the Fig. 1 that the peak at 190 cm^{-1} in the spectrum at 1 atm separates into two peaks with increasing pressure. This observation is consistent with the results of the vibrational mode calculation, in

238 which at least A_g and B_{3g} modes overlap around 190 cm^{-1} (Table 4). The detailed results on the
239 vibrational frequencies vs. pressure of $CaAl_2O_4$ CF are given in Fig. 2. The vibrational frequencies
240 increased with increasing pressure. Most of them drifted linearly up to about 20 GPa. However, the
241 pressure dependences on frequency for the peaks at 351, 399 and 459 cm^{-1} at 1 atm obviously show
242 a kink at about 10 GPa. Such kinks in the frequency vs. pressure relation also have been reported in
243 earlier similar high-pressure Raman spectroscopy experiments, e.g., the study of forsterite reported
244 by Chopelas (1990). The peak at 351 cm^{-1} have been assigned to A_g modes with translation of Al^{3+}
245 and Ca^{2+}. On the other hand, the peaks 399 and 459 cm^{-1} have been assigned to B_{2g} or B_{3g} mode
246 with deformation of AlO_6 octahedra along the *c*-axis. No similarity was found in the movements of
247 atoms between the two groups, which would explain the common occurrenceof kinks at around 10
248 GPa. In the study by Chopelas (1990), the pressure medium of the mixture of methanol and ethanol,
249 which solidified at about 10 GPa, was used and the kinks in the frequency-pressure relations were
250 observed between 8 and 10 GPa. Since the same pressure medium was used in this study, it is likely
251 that non-hydrostatic compression above 10 GPa affected the pressure dependences of the
252 frequencies due to the solidification of the pressure medium.

253 In $MgAl_2O_4$ CF, typical high-pressure Raman spectra are shown in Fig. 3, together with the
254 ambient pressure spectrum. Peaks measured at 13.9 and 17.4 GPa are broader than the
255 corresponding ones at 5.4 and 9.0 GPa. These observations are similar to those of $CaAl_2O_4$ CF. The
256 broadening of the peaks can be explained by the effect of non-hydrostatic compression from the
257 solidification of the methanol–ethanol pressure medium. The frequency vs. pressure data are plotted

in Fig. 4. The peaks at 215, 255, 282, 381, 452 cm^{-1} at 1 atm could not be detected above 10 GPa due to the weak intensity and broadening as described earlier. We can see the kinks in the frequency–pressure relations for the peaks at 174, 340, 444 cm^{-1} at 1 atm. They can be also caused by the non-hydrostatic compression in the solidified pressure medium because these kinks are positioned around 10 GPa. Except for them, the frequencies of the other peaks increased linearly with increasing pressure up to 18 GPa.

Mode Grüneisen parameters

Using the pressure derivative of a vibrational frequency v_i for a mode i, $(\partial v_i/\partial P)_T$, a mode Grüneisen parameter (γ_i) can be obtained using the following equation:

$$\gamma_i = \frac{K_{0,298}}{v_{0i}}\left(\frac{\partial v_i}{\partial P}\right)_T \quad (2)$$

where $K_{0,298}$ and v_{0i} represent isothermal bulk modulus and vibrational frequency of mode i at ambient conditions, respectively. The v_{0i} values determined by the Raman spectroscopy at ambient pressure in this study, listed in Table 1, were used for the calculations. $K_{0,298}$ for $MgAl_2O_4$ CF of 205(6) GPa reported by Sueda et al. (2009) was adopted. As $K_{0,298}$ for $CaAl_2O_4$ CF has not yet been determined, it was estimated as follows. We used the relationship between $K_{0,298}$ and a volume at ambient conditions (V_{298}) reported by Anderson and Anderson (1970), $[K_{0,298}\cdot V_{298}]x = Cx$, in the same way as that carried out in Kojitani et al. (2003), where C is a constant and x signifies a crystal structure. In the calculation, $K_{0,298}$ by Sueda et al. (2009) and V_{298} by Kojitani et al. (2007) for

278 $MgAl_2O_4$ CF and that of $K_{0,298}$ and V_{298} for $CaFe_2O_4$ reported by Merlini et al. (2010) were used.
279 $K_{0,298}$ for $CaAl_2O_4$ CF was estimated to be 183 GPa from the averaged C value. The $(\partial v_i/\partial P)_T$ is a
280 slope of a frequency vs. pressure plot. The slopes were determined by fitting a linear equation to the
281 data up to 10 GPa using the least squares method because of the hydrostatic condition at pressures
282 lower than 10 GPa.

283 In Table 1, the determined $(\partial v_i/\partial P)_T$ and γ_i are tabulated. A total of 18 mode Grüneisen
284 parameters was obtained for $MgAl_2O_4$ CF. A comparison of the γ_i values of $MgAl_2O_4$ CF with the
285 modes assigned by the DTF calculations presented in Table 3 suggests that the modes including the
286 translation of Mg^{2+} as the main movement of ions show the γ_i of 1.8–2.3 (except for peak #1), and
287 that the modes in which translations of Al^{3+} are primary have γ_i of 1.3–1.6. In the frequency range
288 of 400–450 cm^{-1}, only peak #11 indicates higher γ_i of 1.58(9) than those of peaks #9, #10, #12, and
289 #13 (1.2–1.3). The vibrational mode of peak #11 was assigned to translations of Al^{3+} and Mg^{2+}. On
290 the other hand, those of peaks #9, #10, #12, and #13 were assigned to deformations of AlO_6
291 octahedra. These results confirm the mode assignments derived from vibrational mode calculation.
292 The peaks with frequencies higher than 500 cm^{-1} show γ_i of 0.9–1.3. Their main modes are
293 deformation of AlO_6 octahedra. The modes with AlO_6 deformations from 400 to 500 cm^{-1} include
294 B_{2g} and B_{3g} symmetry, in which displacement of oxygens is along the *c*-axis. Most of the modes of
295 the AlO_6 deformations with frequency higher than 500 cm^{-1} have A_g or B_{1g} symmetry, in which
296 oxygen atoms vibrate in the directions parallel to the *a*-*b* plane. This suggests that the modes with
297 AlO_6 deformations in B_{2g} or B_{3g} could give lower frequency and higher γ_i than those in A_g or B_{1g}. It

298 is expected that less compressibility along the *c*-axis direction caused by edge-sharing connections
299 of AlO_6 octahedra might affect the γ_i values.

300 From the high-pressure Raman spectroscopy of $CaAl_2O_4$ CF, 26 mode Grüneisen parameters
301 were determined, as shown in Table 1. The modes including translations of only Ca^{2+} without
302 deformations of AlO_6 octahedra, i.e., peaks #1 and #8, indicate relatively small γ_i of 0.7–0.9. Peak
303 #2, separating from peak #1 with increasing pressure, is probably assigned to the A_g mode, because
304 it includes not only translations of Ca^{2+} and Al^{3+}, but also the deformation of AlO_6 octahedra. In the
305 frequency range of 220–390 cm^{-1}, major peaks can be assigned to translations of Ca^{2+} and/or Al^{3+}
306 combined with deformations of AlO_6 octahedra. They show γ_i of 1.4–1.8. The results suggest that γ_i
307 of the peaks containing translations of Ca^{2+} are slightly smaller than those corresponding to the
308 similar ones of $MgAl_2O_4$ CF. This tendency is in good agreement with that of mode Grüneisen
309 parameters for Mg_2GeO_4 and Ca_2GeO_4 olivines reported by Fiquet et al. (1992). It is implied that
310 divalent cations with larger ionic size result in smaller γ_i for a mode, which includes a translation of
311 the divalent cation. Peaks in the range of 390–550 cm^{-1} were assigned to modes with deformations
312 of AlO_6 octahedra. They provide γ_i of 1.1–1.3. Particularly, some modes in B_{2g} and B_{3g} indicate
313 much larger values of 1.7–1.8 (i.e., peaks #12 and #16). At frequencies higher than 550 cm^{-1}, γ_i
314 values of the peaks assigned to modes with deformations of AlO_6 octahedra in A_g or B_{1g} symmetry
315 were obtained to be 0.8–1.0, which are similar to those of the peaks with frequencies higher than
316 500 cm^{-1} for $MgAl_2O_4$ CF.

317

318 Estimation of thermal Grüneisen parameters

319

320 The thermal Grüneisen parameters (γ_{th}) were calculated by the weighted average of the mode
321 Grüneisen parameters (γ_i) determined experimentally, using the following equation (e.g., Chopelas
322 1996):

323 $$\gamma_{th} = \frac{\sum_i C_{V_i} \cdot \gamma_i}{\sum_i C_{V_i}} \quad (3)$$

324 where C_{Vi} is a harmonic heat capacity contribution of each mode i. The C_{Vi} values were estimated
325 from the Einstein function:

326 $$C_{V_i} = k \cdot \left(\frac{h\nu_i}{kT}\right)^2 \exp\left(\frac{h\nu_i}{kT}\right) \Big/ \left[\exp\left(\frac{h\nu_i}{kT}\right) - 1\right]^2 \quad (4)$$

327 where ν_i, is the vibrational frequency of mode i given in 1/s, T is the temperature in K, while h and k
328 are the Plank and Boltzmann constants, respectively. In this study, we calculated C_{Vi} using ν_i
329 observed at ambient conditions and also expected by the vibrational mode calculations.

330 The γ_{th} value of $CaAl_2O_4$ CF was determined to be 1.30(2) using the 26 γ_i presented in Table 1 at
331 300 K. If the contributions of unobserved Raman active modes and Raman inactive modes (i.e.,
332 ungerade modes) are taken into account by assuming that modes with similar atomic motions have
333 the same γ_i, γ_{th} by γ_i for all modes listed in Table 4 is estimated to be 1.31(3). The γ_{th} by all modes
334 was found to be the same as that by only observed Raman modes within the uncertainties. Similarly,
335 γ_{th} of $MgAl_2O_4$ CF was determined to be 1.50(4) by adopting the 18 observed γ_i in Table 1. If γ_i for
336 all the modes shown in Table 3 are used, it is estimated as 1.50(5) from the same assumption in

337 $CaAl_2O_4$ CF. These results suggest that the values for γ_{th} obtained from observed Raman active
338 modes already give a good estimate of γ_{th} from all modes.

339

340 Heat capacity calculation

341

342 Isochoric heat capacities (C_V) of $MgAl_2O_4$ CF and $CaAl_2O_4$ CF were calculated using Kieffer
343 model (Kieffer 1979a, 1979b). The VDoS models adopted by Kojitani et al. (2003) were modified
344 by considering the frequencies of all the modes obtained by the vibrational mode calculations, in
345 addition to the observed Raman data. The VDoS models used in this study are tabulated in Table 5
346 and are also illustrated in Fig. 5. The results of the C_V calculations are shown in Table 6. C_V of
347 $CaAl_2O_4$ CF was found to be slightly larger than that of $MgAl_2O_4$ CF in the whole temperature
348 range. This is explained by the higher density of states in the first optic continuum and the lower
349 cutoff frequencies of the acoustic modes for $CaAl_2O_4$ CF than those for $MgAl_2O_4$ CF. Above 1400
350 K, their C_V were close to the Dulong-Petit limit (3nR = 174.6 J/mol K, where n is the number of
351 atoms per chemical formula and R is the gas constant). The present C_V's for both $MgAl_2O_4$ CF and
352 $CaAl_2O_4$ CF are larger than those by Kojitani et al. (2003), respectively, at each temperature,
353 because the optic continua of the present VDoS models distribute in the lower frequency region
354 than those of the previous ones.

355 Using the obtained C_V, γ_{th} can be calculated from the Grüneisen relation equation:

356 $$\gamma_{th} = \frac{\alpha K_{0T} V_T}{C_V} \quad (5)$$

where α, K_{0T}, and V_T are thermal expansivity, isothermal bulk modulus, and volume, respectively. For $MgAl_2O_4$ CF, C_V at 300 K of 112.3(8) J/mol determined in this study, α of $1.96(13)\times10^{-5}+1.64(24)\times10^{-8}T$ /K, and $K_{0,298}$ of 205(6) GPa by Sueda et al. (2009), and V_{298} of 36.136(3) cm^3/mol by Kojitani et al. (2007) provide γ_{th} of 1.62(10), where the uncertainty was evaluated by the propagation of the experimental errors. Our γ_{th} obtained from γ_i is in agreement with this value. This suggests that γ_{th} can be well restricted from the mode Grüneisen parameters determined by spectroscopy.

Isobaric heat capacity (C_P) is calculated by the relationship between C_P and C_V, generally expressed by the equation:

$$C_P = C_V + \alpha^2 K_{0T} V_T T . \quad (6)$$

The second term represents the anharmonic effect on C_P. K_{0T} was calculated using the equation:

$$K_{0T} = K_{0,298} + \left(\frac{\partial K_{0T}}{\partial T}\right)_P \cdot (T - 298) . \quad (7)$$

Since the temperature derivative of K_{0T} for $CaAl_2O_4$ CF has not yet been determined, it was assumed to be the same as that for $MgAl_2O_4$ CF (−0.030 GPa/K) reported by Sueda et al. (2009). V_T was obtained from the equation:

$$V_T = V_{298} \cdot \exp\left(\int_{298}^{T} \alpha dT\right) . \quad (8)$$

α in Eqs. (6) and (8) was calculated from the modified Eq. (5):

$$\alpha = \frac{\gamma_{th} C_V}{K_{0T} V_T} \quad (9)$$

where the γ_{th} was assumed to be constant because mantle constituent materials show almost constant γ_{th} (e.g., Anderson and Isaak 1995). The α calculation was started with the initial V_T of

377 constant V_{298}. The calculated α was substituted for that in Eq. (8). Then, the obtained V_T was used to
378 calculate a new α. Total three times iteration of the procedure gave the final α. The polynomial
379 expressions of the calculated α's are shown in Table 7.

380 The results of the C_P calculations are listed in Table 6, compared with the previous calculations
381 by Kojitani et al. (2003). The C_P expressions using the equation of Robie and Hemingway (1995)
382 are given in Table 8. The present C_P for $MgAl_2O_4$ CF is slightly smaller than that by Kojitani et al.
383 (2003) above 200 K due to the smaller anharmonic effect calculated in this study, mainly derived
384 from the smaller $K_{0,298}$ of 205 GPa by Sueda et al. (2005) than 241 GPa by Yutani et al. (1997)
385 which was used in Kojitani et al. (2003). When the present C_P for $MgAl_2O_4$ CF and $CaAl_2O_4$ CF are
386 compared, the former is smaller than the latter at the same temperature up to 1100 K. However, in
387 the temperature range of > 1100 K, the relation is reversed. This is caused by the larger γ_{th} of
388 $MgAl_2O_4$ CF than that of $CaAl_2O_4$ CF. In addition, the γ_{th} for $CaAl_2O_4$ CF of 1.31 also results in the
389 smaller calculated C_P of this study than that of Kojitani et al. (2003) above 1000 K. The obtained
390 C_P's can be applied to the calculation of the vibrational entropy at T K from the following equation:

391 $$S^\circ_T = \int_0^T \frac{C_P}{T} dT \quad . \qquad (10)$$

392 The vibrational entropies at 298 K ($S°_{298}$) for $MgAl_2O_4$ CF and $CaAl_2O_4$ CF were calculated to be
393 85.3 and 95.7 J/mol K, respectively.

394 The calculated C_P for $CaAl_2O_4$ CF in this study is compared with experimental data by Kojitani
395 et al. (2003) in Fig. 6. The calculated C_P agrees well with the measured ones below 430 K. Above
396 430 K, although the calculated C_P is consistent with the measured ones within the uncertainties, the

397 measured C_P's are systematically 3−4% higher than the calculated values. It should be mentioned
398 that the measurement conditions of the DSC measurement by Kojitani et al. (2003) were changed at
399 350 K from the heating rate of 6 K/min with 5 K interval to 7 K/min with 10 K interval. The change
400 of the conditions might have affected the measured C_P above 430 K. These facts imply that the
401 re-measurement of high-temperature heat capacity for $CaAl_2O_4$ CF would be desirable.
402
403
404 Acknowledgments
405 We thank H. Kagi for instruction of high-pressure experimental technique using a diamond
406 anvil cell high-pressure apparatus and anonymous reviewers for constructive reviews. This work
407 was supported by Grants-in-Aid (no. 21540497 to H.K.) from Japan Society for the Promotion of
408 Science and the Austrian Ministry of Science BMWF, as a part of the UniInfrastrukturprogramm of
409 the Forschungsplattform Scientific Computing at LFU Innsbruck.
410
411
412 References
413
414 Adamo, C. and Barone, V. (1999) Toward reliable density functionals without adjustable
415 parameters: the PBE0 model. Journal of Chemical Physics, 110, 6158−6170.
416 Akaogi, M., Hamada, Y., Suzuki, T., Kobayashi, M., and Okada, M. (1999) High pressure

transitions in the system $MgAl_2O_4$–$CaAl_2O_4$: a new hexagonal aluminous phase with implication for the lower mantle. Physics of the Earth and Planetary Interiors, 115, 67–77.

Anderson, D.L. and Anderson, O.L. (1970) The bulk modulus–volume relationship for oxides. Journal of Geophysical Research, 75, 3494–3500.

Anderson, O.L. and Isaak, D.G. (1995) Elastic constants of mantle minerals at high temperature, In T.J. Ahrens, Ed., Rock physics and crystallography: a handbook of physical constants, p. 64–97, AGU Reference shelf 2, American Geophysical Union, Washington, D.C.

Angel, R.J., Bujak, M., Zhao, J., Gatta, G.D., and Jacobsen, S.D. (2007) Effective hydrostatic limits of pressure media for high-pressure crystallographic studies. Journal of Applied Crystallography, 40, 26–32.

Catti, M., Dovesi, R., Pavese, A., and Saunders, V.R. (1991) Elastic constants and electronic structure of fluorite (CaF_2): an ab initio Hartree-Fock study. Journal of Physics: Condensed Matter, 3, 4151–4164.

Chopelas, A. (1990) Thermal properties of forsterite at mantle pressures derived from vibrational spectroscopy. Physics and Chemistry of Minerals, 17, 149–156.

Chopelas, A. (1996) Thermal expansivity of lower mantle phases MgO and $MgSiO_3$ perovskite at high pressure derived from vibrational spectroscopy. Physics of the Earth and Planetary Interiors, 98, 3–15.

Dovesi, R., Orlando, R., Civalleri, B., Roetti, C., Saunders, V.R., and Zicovich-Wilson, C.M. (2005) CRYSTAL: a computational tool for the ab initio study of the electronic properties of crystals.

Zeitschrift für Kristallographie, 220, 571−573.

Fiquet, G., Gillet, P., and Richet, P. (1992) Anharmonicity and high-temperature heat capacity of crystals: the examples of Ca_2GeO_4, Mg_2GeO_4 and $CaMgGeO_4$ olivines. Physics and Chemistry of Minerals, 18, 469−479.

Funamori, N., Jeanloz, R., Miyajima, N., and Fujino, K. (2000) Mineral assemblages of basalt in the lower mantle. Journal of Geophysical Research, 105, 2603−26043.

Guignot, N. and Andrault, D. (2004) Equations of state of Na−K−Al host phases and implications for MORB density in the lower mantle, Physics of the Earth and Planetary Interiors, 143−144, 107−128.

Hirose, K., Fei, Y., Ma, Y., and Mao, H.K. (1999) The fate of subducted basaltic crust in the Earth's lower mantle. Nature, 397, 53−56.

Irifune, T. and Ringwood, A.E. (1993) Phase transformations in subducted oceanic crust and buoyancy relationships at depths of 600-800 km in the mantle. Earth and Planetary Science Letters, 117, 101−110.

Kesson, S.E., Fitz Gerald, J.D., and Shelly, J.M.G. (1994) Mineral chemistry and density of subducted basalt crust at lower-mantle pressures. Nature, 372, 767−769.

Kieffer, S.W. (1979a) Thermodynamics and lattice vibrations of minerals: 1. Mineral heat capacities and their relationships to simple lattice vibrational models. Reviews of Geophysics and Space Physics, 17, 1−19.

————— (1979b) Thermodynamics and lattice vibrations of minerals: 3. Lattice dynamics and

an approximation for minerals with application to simple substances and framework silicates. Reviews of Geophysics and Space Physics, 17, 35−59.

Kojitani, H., Nishimura, K., Kubo, A., Sakashita, M., Aoki, K., and Akaogi, M. (2003) Raman spectroscopy and heat capacity measurement of calcium ferrite type $MgAl_2O_4$ and $CaAl_2O_4$. Physics and Chemistry of Minerals, 30, 409−415.

Kojitani, H., Hisatomi, R., and Akaogi, M. (2007) High-pressure phase relations and crystal chemistry of calcium ferrite-type solid solutions in the system $MgAl_2O_4$−Mg_2SiO_4. American Mineralogist, 92, 1112−1118.

Kubo, A. and Akaogi, M. (2000) Post-garnet transitions in the system $Mg_4Si_4O_{12}$−$Mg_3Al_2Si_3O_{12}$ up to 28 GPa: phase relations of garnet, ilmenite and perovskite. Physics of the Earth and Planetary Interiors, 121, 85−102.

Lazic, B., Kahlenberg, V., Konzett, J., and Kaindl, R. (2006) On the polymorphism of $CaAl_2O_4$ – structural investigations of two high pressure modifications. Solid State Sciences, 8, 589−597.

McCarthy, M.I. and Harrison, N.M. (1994) Ab initio determination of the bulk properties of MgO. Physical Review, B 49, 8574−8582.

Merlini, M., Hanfland, M., Gemmi, M., Huotari, S., Simonelli, L., and Strobel, P. (2010) Fe^{3+} spin transition in $CaFe_2O_4$ at high pressure. American Mineralogist, 95, 200−203.

Ono, S., Ito, E., and Katsura, T. (2001) Mineralogy of subducted basaltic crust (MORB) from 25 to 37 GPa, and chemical heterogeneity of the lower mantle. Earth and Planetary Science Letters, 190, 57−63.

Pascale, F., Zicovich-Wilson, C.M., Lopez Gejo, F., Civalleri, B., Orlando, R., and Dovesi, R. (2004) The calculation of vibrational frequencies of crystalline compounds. Journal of Computational Chemistry, 25, 888−897.

Piermarini, G.J., Block, S., Barnett, J.D., and Forman, R.A. (1975) Calibration of the pressure dependence of the R1 ruby fluorescence line to 195 kbar. Journal of Applied Physics, 46, 2774−2780.

Robie, R.A. and Heningway, B.S. (1995) Thermodynamic properties of minerals and related substances at 298.15 K and 1 bar (10^5 Pascals) pressure and at higher temperatures. US Geological Survey Bulletin 2131, 461pp.

Ricolleau, A., Fiquet, G., Addad, A., Menguy, N., Vanni, C., Perrillat, J.-P., Daniel, I., Cardon, H., and Guignot, N. (2008) Analytical transmission electron microscopy study of a natural MORB sample assemblage transformed at high pressure and high temperature. American Mineralogist, 93, 144−153.

Sueda, Y., Irifune, T., Sanehira, T., Yagi, T., Nishiyama, N., Kikegawa, T., and Funakoshi, K. (2009) Thermal equation of state of $CaFe_2O_4$-type $MgAl_2O_4$. Physics of the Earth and Planetary Interiors, 174, 78−85.

Suzuki, T. and Akaogi, M. (1995) Element partitioning between olivine and silicate melt under high pressure. Physics and Chemistry of Minerals, 22, 411−418.

Towler, M.D., Allan, N.L., Harrison, N.M., Saunders, V.R., Mackrodt, W.C., and Apra, E. (1994) An ab initio Hartree-Fock study of MnO and NiO. Physical Review, B50, 5041−5054.

497 Többens, D.M. and Kahlenberg, V. (2011) Improved DFT calculation of Raman spectra of silicates.
498 Vibrational Spectroscopy, 56, 265−272.
499 Yutani, M., Yagi, T., Yusa, H., and Irifune, T. (1997) Compressibility of calcium ferrite-type
500 $MgAl_2O_4$. Physics and Chemistry of Minerals, 24, 340−344.
501

502 Figure captions

503

504 Figure 1. Raman spectra of calcium ferrite-type $CaAl_2O_4$ observed at 1 atm, 6.2, 9.3, 15.3,
505 and 17.4 GPa. (a) Spectra in a whole range and (b) enlarged spectra in a range of 150−420
506 cm^{-1}.

507

508 Figure 2. Raman frequencies vs. pressure plot of calcium ferrite-type $CaAl_2O_4$. Solid lines
509 show trends of the observed data. These trend lines are illustrated separately around 10 GPa,
510 at which a used pressure medium solidifies.

511

512 Figure 3. Raman spectra of calcium ferrite-type $MgAl_2O_4$ observed at 1 atm, 5.4, 9.0, 13.7,
513 and 17.1 GPa. (a) Spectra in a whole range and (b) enlarged spectra in a range of 150−420
514 cm^{-1}.

515

516 Figure 4. Raman frequencies vs. pressure plot of calcium ferrite-type $MgAl_2O_4$. Solid lines
517 show trends of the observed data. These trend lines are illustrated separately around 10 GPa
518 because of the solidification of the pressure medium.

519

520 Figure 5. Vibrational density of states models of (a) calcium ferrite-type $MgAl_2O_4$ and (b)
521 calcium ferrite-type $CaAl_2O_4$. Boxes represent optic continua. Numerals in the boxes

522 indicate fractions of modes in the optic continua. Vertical lines show cutoff frequencies of
523 transversal acoustic modes (TA) and longitudinal acoustic modes (LA).

524

525 Figure 6. Isobaric heat capacity of calcium ferrite-type $CaAl_2O_4$. Solid line shows the
526 calculated isobaric heat capacity in this study. Open circles are calorimetric data by
527 Kojitani et al. (2003). Error bars mean the standard deviation.

528
529

Table 1. Raman peaks observed at 1 atm, pressure dependences of peak positions and mode Grüneisen parameters of calcium ferrite-type $MgAl_2O_4$ ($MgAl_2O_4$ CF) and calcium ferrite-type $CaAl_2O_4$ ($CaAl_2O_4$ CF)

	$MgAl_2O_4$ CF				$CaAl_2O_4$ CF			
Peak No.	v_{0i} (cm^{-1})	$(\partial v_i/\partial P)_T$ (cm^{-1}/GPa)	γ_i		Peak No.	v_{0i} (cm^{-1})	$(\partial v_i/\partial P)_T$ (cm^{-1}/GPa)	γ_i
1	174	1.13(10)	1.33(12)		1	189	0.88(7)	0.85(7)
2	215	2.38(17)	2.27(17)		2	189	2.14(14)	2.07(14)
3	244	2.31(15)	1.94(14)		3	222	1.85(21)	1.52(18)
4	255	2.30(16)	1.84(14)		4	227	1.63(5)	1.32(5)
5	282	2.94(43)	2.14(32)		5	243	1.88(10)	1.42(8)
6	340	2.44(12)	1.47(8)		6	260	1.51(15)	1.06(11)
7	365	2.39(26)	1.34(15)		7	278	2.08(18)	1.37(12)
8	381	2.81(31)	1.52(17)		8	301	1.24(19)	0.76(12)
9	408	2.71(21)	1.36(11)		9	306	1.99(10)	1.19(6)
10	418	2.42(13)	1.19(7)		10	351	3.41(3)	1.78(4)
11	438	3.38(17)	1.58(9)		11	384	2.97(7)	1.42(4)
12	444	2.77(18)	1.28(9)		12	399	3.95(5)	1.81(4)
13	452	2.88(14)	1.31(7)		13	422	3.04(6)	1.32(4)
14	474	−	−		14	445	3.16(5)	1.30(3)
15	502	2.76(12)	1.13(6)		15	451	3.22(8)	1.31(4)
16	566	−	−		16	459	4.28(7)	1.71(4)
17	603	3.26(18)	1.11(7)		17	483	3.52(8)	1.33(4)
18	644	−	−		18	494	3.15(6)	1.17(3)
19	683	3.19(17)	0.96(6)		19	512	3.68(4)	1.31(3)
20	708	3.22(9)	0.93(4)		20	522	3.67(5)	1.29(3)
21	747	3.32(24)	0.91(7)		21	543	3.36(5)	1.13(3)
22	816	−	−		22	571	2.74(7)	0.88(3)
23	857	−	−		23	614	2.99(6)	0.89(2)
24	1106	−	−		24	641	3.23(4)	0.92(2)
					25	704	3.40(4)	0.88(2)
					26	734	4.06(9)	1.01(3)
					27	756	−	−
					28	925	−	−
					29	1086	−	−

v_{0i}: Raman peak positions measured at ambient conditions.

γ_i: Mode Grüneisen parameter.

$\gamma_i = K_{0,298}(\partial v_i/\partial P)_T/v_{0i}$ where $K_{0,298}$ is an isothermal bulk modulus at ambient conditions. The $K_{0,298}$ values for $MgAl_2O_4$ CF and $CaAl_2O_4$ CF were 205 GPa determined by Sueda

569 et al. (2009) and 183 GPa estimated in this study, respectively.
570

Table 2. Comparisons between observed and energy-optimized crystallographic data of calcium ferrite-type $MgAl_2O_4$ and $CaAl_2O_4$

		Obs.	Calc.	Deviation (%)
$MgAl_2O_4$ CF				
a (Å)		9.9498(6)	9.9731	0.23
b (Å)		8.6468(6)	8.6738	0.31
c (Å)		2.7901(2)	2.7967	0.24
V(Å^3)		240.02(2)	241.93	0.80
Mg	*x*	0.3503(4)	0.3474	0.83
	y	0.7576(6)	0.7557	0.25
	z	1/4	1/4	−
Al1	*x*	0.3854(4)	0.3838	0.42
	y	0.4388(5)	0.4408	0.46
	z	1/4	1/4	−
Al2	*x*	0.8964(3)	0.8965	0.01
	y	0.4159(4)	0.4139	0.48
	z	1/4	1/4	−
O1	*x*	0.8344(7)	0.8313	0.37
	y	0.2005(8)	0.2015	0.50
	z	1/4	1/4	−
O2	*x*	0.5279(7)	0.5288	0.17
	y	0.1201(6)	0.1202	0.08
	z	1/4	1/4	−
O3	*x*	0.2150(7)	0.2161	0.51
	y	0.5357(8)	0.5351	0.11
	z	1/4	1/4	−
O4	*x*	0.5709(6)	0.5708	0.02
	y	0.4089(7)	0.4120	0.76
	z	1/4	1/4	−
$CaAl_2O_4$ CF				
a (Å)		10.31550(6)	10.3476	0.31
b (Å)		8.92004(5)	8.9344	0.16
c (Å)		2.87129(1)	2.8830	0.41
V(Å^3)		264.201(2)	266.53	0.88
Ca	*x*	0.3438(1)	0.3437	0.03
	y	0.7576(1)	0.7576	0.00

		z	1/4	1/4	–
	Al1	*x*	0.3901(1)	0.3896	0.13
		y	0.4372(2)	0.4376	0.09
		z	1/4	1/4	–
	Al2	*x*	0.8973(1)	0.8973	0.00
		y	0.4183(2)	0.4194	0.26
		z	1/4	1/4	–
	O1	*x*	0.8461(3)	0.8459	0.02
		y	0.2034(3)	0.2036	0.10
		z	1/4	1/4	–
	O2	*x*	0.5188(3)	0.5197	0.17
		y	0.1154(3)	0.1143	0.95
		z	1/4	1/4	–
	O3	*x*	0.2149(3)	0.2153	0.19
		y	0.5273(3)	0.5260	0.25
		z	1/4	1/4	–
	O4	*x*	0.5706(3)	0.5721	0.26
		y	0.4226(3)	0.4231	0.12
		z	1/4	1/4	–

CF: Calcium ferrite.

Observed lattice parameters and atomic positions of $MgAl_2O_4$ CF and $CaAl_2O_4$ CF are from Kojitani et al. (2007) and Lazic et al. (2006), respectively.

Table 3. Results of density functional theory calculation of lattice vibrational modes and assigned mode Grüneisen parameters for calcium ferrite-type $MgAl_2O_4$

Mode No.	ν_{0i}^{calc} (cm^{-1})	ν_{0i}^{obs} (cm^{-1})	Symmetry	Mode assignment	γ_i
Raman active modes					
1	163	174	B_{2g}	T(Mg: z)	1.33
2	168	174	A_g	T(Mg: x), T(Al: y), D(AlO_6: x-y)	1.33
3	171	174	B_{3g}	T(Mg: z)	1.33
4	206	208	A_g	T(Mg: y), T(Al: y), D(AlO_6: x-y)	2.27*
5	208	208	B_{1g}	D(AlO_6: x-y), T(Al: x-y), T(Mg: y)	2.27*
6	212	215	B_{2g}	D(AlO_6: z), T(Al: z)	2.27
7	241	244	A_g	T(Mg: x), T(Al: x-y), D(AlO_6: x-y)	1.94
8	258	255	B_{3g}	T(Al: z), D(AlO_6: z)	1.84
9	267	−	B_{1g}	T(Mg: x-y), T(Al: y), D(AlO_6: x-y)	2.14*
10	281	282	B_{3g}	T(Al: z), D(AlO_6: z)	2.14
11	284	282	B_{1g}	T(Mg: x), T(Al: x-y), D(AlO_6: x-y)	2.14
12	311	−	B_{2g}	T(Al: z), D(AlO_6: z)	1.84*
13	338	340	A_g	T(Al: x), D(AlO_6: x-y), T(Mg: y)	1.47
14	362	364	A_g	T(Al: x-y), D(AlO_6: x-y), T(Mg: x)	1.34
15	368	364	B_{1g}	T(Al: x), D(AlO_6: x-y)	1.34
16	388	381	B_{1g}	T(Al: y), T(Mg: y), D(AlO_6: x-y)	1.52
17	414	408	B_{2g}	D(AlO_6: z)	1.36
18	420	418	B_{3g}	D(AlO_6: z)	1.19
19	437	438	B_{1g}	T(Al: y), T(Mg: x), D(AlO_6: x-y)	1.58
20	441	444	B_{3g}	D(AlO_6: z)	1.28
21	449	452	B_{2g}	D(AlO_6: z)	1.31
22	452	452	A_g	T(Al: x-y), D(AlO_6: x-y)	1.31
23	465	474	B_{1g}	D(AlO_6: x-y), T(Al: x-y)	1.13*
24	481	−	A_g	D(AlO_6: x-y), T(Mg: y), T(Al: x-y)	1.13*
25	490	502	B_{2g}	D(AlO_6: z)	1.13
26	497	502	A_g	D(AlO_6: x-y), T(Al: x-y)	1.13
27	498	502	B_{3g}	D(AlO_6: z)	1.13
28	514	−	B_{1g}	D(AlO_6: x-y), T(Al: x-y)	1.13*
29	528	528	A_g	T(Al: y, x), D(AlO_6: x-y), T(Mg: y)	1.31*
30	569	566	B_{1g}	T(Al: x), D(AlO_6: x-y)	1.31*
31	597	603	A_g	D(AlO_6: x-y), T(Al: x)	1.11
32	604	603	B_{3g}	D(AlO_6: z)	1.11
33	609	603	B_{2g}	D(AlO_6: z)	1.11
34	634	644	A_g	D(AlO_6: x-y), T(Al: x-y)	1.11*
35	643	644	B_{1g}	D(AlO_6: x-y), T(Al: x-y)	1.11*

675	36	672	683	B_{1g}	D(AlO_6: x-y), T(Al: x-y)	0.96
676	37	682	683	A_g	D(AlO_6: x-y), T(Al: x)	0.96
677	38	704	708	A_g	D(AlO_6: x-y), T(Al: x-y)	0.93
678	39	710	708	B_{1g}	D(AlO_6: x-y)	0.93
679	40	740	747	B_{1g}	D(AlO_6: x-y), T(Al: x-y), T(Mg: y)	0.91
680	41	817	816	A_g	D(AlO_6: x-y), T(Al: x)	0.96*
681	42	856	857	B_{1g}	D(AlO_6: x-y), T(Al: x)	0.96*
682						
683	IR active and optically non-active modes					
684	43	119		B_{3u}	T(Mg: x-y), T(Al: x), D(AlO_6: x-y)	1.33*
685	44	141		A_u	T(Mg: z), T(Al: z), D(AlO_6: z)	2.27*
686	45	155		A_u	T(Mg: z), T(Al: z), D(AlO_6: z)	2.27*
687	46	163		B_{2u}	T(Mg: y), T(Al: y), D(AlO_6: y)	2.27*
688	47	176		B_{1u}	T(Mg: z), T(Al: z)	1.84*
689	48	209		A_u	T(Mg: z), T(Al: z) , D(AlO_6: z)	1.84*
690	49	214		B_{3u}	T(Mg: x-y), T(Al: x-y), D(AlO_6: x-y)	1.94*
691	50	229		B_{1u}	D(AlO_6: z), T(Mg: z), T(Al: z)	2.27*
692	51	231		B_{2u}	T(Mg: y), T(Al: x-y), D(AlO_6: x-y)	2.14*
693	52	273		B_{3u}	T(Mg: x-y), T(Al: x), D(AlO_6: x-y)	2.14*
694	53	285		B_{2u}	T(Mg: x), D(AlO_6: x), T(Al: x)	2.14*
695	54	301		B_{3u}	T(Al: x), D(AlO_6: x-y), T(Mg: y)	1.47*
696	55	335		B_{2u}	T(Al: x-y), D(AlO_6: x-y), T(Mg: x-y)	1.34*
697	56	352		B_{2u}	T(Al: x-y), D(AlO_6: x-y), T(Mg: y)	1.47*
698	57	378		B_{3u}	T(Al: x), D(AlO_6: x-y), T(Mg: y)	1.47*
699	58	379		B_{1u}	D(AlO_6: z)	1.36*
700	59	386		B_{2u}	D(AlO_6: x-y), T(Al: x-y), T(Mg: x-y)	1.34*
701	60	387		A_u	D(AlO_6: z)	1.31*
702	61	398		B_{1u}	D(AlO_6: z)	1.31*
703	62	402		A_u	D(AlO_6: z)	1.31*
704	63	416		B_{3u}	D(AlO_6: x-y), T(Al: x-y), T(Mg: x-y)	1.58*
705	64	438		A_u	D(AlO_6: z), T(Al: z)	1.13*
706	65	443		B_{1u}	D(AlO_6: z)	1.13*
707	66	469		B_{3u}	T(Al: x, y), D(AlO_6: x-y), T(Mg: x)	1.31*
708	67	484		B_{2u}	T(Al: x-y), D(AlO_6: x-y)	1.31*
709	68	493		B_{3u}	D(AlO_6: x-y), T(Al: x-y), T(Mg: y)	1.13*
710	69	524		B_{2u}	D(AlO_6: x-y), T(Al: x-y), T(Mg: x)	1.13*
711	70	559		B_{2u}	T(Al: x), D(AlO_6: x-y)	1.31*
712	71	583		B_{3u}	T(Al: x-y), D(AlO_6: x-y)	1.31*
713	72	595		A_u	D(AlO_6: z)	1.11*
714	73	597		B_{1u}	D(AlO_6: z)	1.11*

74	599	B_{2u}	D(AlO_6: x-y), T(Al: x)	0.96*
75	600	B_{3u}	D(AlO_6: x-y)	0.93*
76	712	B_{2u}	D(AlO_6: x-y)	0.93*
77	725	B_{3u}	D(AlO_6: x-y), T(Al: y)	0.96*
78	762	B_{3u}	D(AlO_6: x-y), T(Al: x)	0.96*
79	774	B_{2u}	D(AlO_6: x-y), T(Al: x-y), T(Mg: y)	0.91*
80	818	B_{2u}	D(AlO_6: x-y), T(Al: x-y)	0.96*
81	825	B_{3u}	D(AlO_6: x), T(Al: x)	0.96*
82	0	B_{2u}	T(Mg, Al, O: x), acoustic mode	
83	0	B_{3u}	T(Mg, Al, O: y), acoustic mode	
84	0	B_{1u}	T(Mg, Al, O: z), acoustic mode	

Symmetries are of space group *Pbnm*.

T: translation; D: deformation.

The x, y, and z, which are identical to crystal axes *a*, *b*, and *c* of the calcium ferrite structure with the space group *Pbnm*, respectively, show the direction of atomic displacements.

* Values were estimated by assuming that modes with similar atomic motions have the same mode Grüneisen parameter.

Table 4. Results of density functional theory calculation of lattice vibrational modes and assigned mode Grüneisen parameters for calcium ferrite-type $CaAl_2O_4$

Mode No.	ν_{0i}^{calc} (cm^{-1})	ν_{0i}^{obs} (cm^{-1})	Symmetry	Mode assignment	γ_i
Raman active modes					
1	180	189	B_{2g}	T(Ca: z)	0.85
2	184	189	A_g	T(Ca: x-y), T(Al: y), D(AlO_6: x-y)	2.07
3	187	189	B_{3g}	T(Ca: z)	0.85
4	221	222	A_g	T(Ca: x-y), T(Al: x-y), D(AlO_6: x-y)	1.52
5	227	227	B_{2g}	T(Al: z), D(AlO_6: z), T(Ca: z)	1.32
6	239	243	B_{1g}	T(Ca: x-y), T(Al: x-y), D(AlO_6: x-y)	1.42
7	256	260	B_{3g}	T(Al: z), D(AlO_6: z)	1.06
8	257	260	B_{1g}	T(Ca: x), T(Al: x-y), D(AlO_6: x-y)	1.06
9	265	−	B_{1g}	T(Ca: y), T(Al: y), D(AlO_6: x-y)	1.06*
10	274	278	B_{3g}	T(Al: z), D(AlO_6)	1.37
11	296	301	A_g	T(Ca: y), T(Al: x-y), D(AlO_6: x-y)	0.76
12	298	306	B_{2g}	T(Al: z), D(AlO_6: z)	1.19
13	344	351	A_g	T(Al: x), D(AlO_6: x-y), T(Ca: x)	1.78
14	365	−	B_{1g}	T(Al: x, y), D(AlO_6: x-y), T(Ca: x)	1.78*
15	382	384	A_g	T(Al: x-y), D(AlO_6: x-y)	1.42
16	383	384	B_{1g}	T(Al: x), D(AlO_6: x-y)	1.42
17	394	399	B_{2g}	D(AlO_6: z)	1.81
18	396	399	B_{3g}	D(AlO_6: z)	1.81
19	423	422	A_g	T(Al: x-y), D(AlO_6: x-y)	1.32
20	426	422	B_{1g}	T(Al: y), D(AlO_6: x-y), T(Ca: x)	1.32
21	441	445	B_{1g}	D(AlO_6: x-y), T(Al: x-y)	1.30
22	442	445	A_g	D(AlO_6: x-y), T(Al: y)	1.30
23	450	451	B_{3g}	D(AlO_6: z)	1.31
24	455	451	A_g	D(AlO_6: x-y)	1.31
25	456	459	B_{2g}	D(AlO_6: z)	1.71
26	480	483	B_{1g}	D(AlO_6: x-y), T(Al: x)	1.34
27	496	494	A_g	D(AlO_6: x-y), T(Al: x, y)	1.17
28	510	512	B_{2g}	D(AlO_6: z)	1.31
29	519	522	B_{3g}	D(AlO_6: z)	1.29
30	536	−	B_{3g}	D(AlO_6: z)	1.29*
31	542	543	B_{2g}	D(AlO_6: z)	1.13
32	542	543	B_{1g}	D(AlO_6: x-y), T(Al: x-y)	1.13
33	567	571	A_g	D(AlO_6: x-y), T(Al: x-y)	0.88
34	610	614	A_g	T(Al: x-y), D(AlO_6: x-y)	0.89
35	616	614	B_{1g}	D(AlO_6: x-y)	0.89

773	36	628	–	B_{1g}	D(AlO_6: x-y), T(Al: x, y)	0.92*
774	37	644	641	A_g	D(AlO_6: x-y), T(Al: x)	0.92
775	38	700	704	A_g	D(AlO_6: x-y)	0.88
776	39	707	704	B_{1g}	D(AlO_6: x-y) , T(Al: x, y)	0.88
777	40	709	704	B_{1g}	D(AlO_6: x-y)	0.88
778	41	731	734	A_g	D(AlO_6: x-y), T(Al: x)	1.01
779	42	753	756	B_{1g}	D(AlO_6: x-y), T(Al: x)	0.92*
780						
781	IR active and optically non-active modes					
782	43	146		A_u	T(Ca: z), T(Al: z), D(AlO_6: z)	2.07*
783	44	152		B_{2u}	T(Ca: y), T(Al: x, y), D(AlO_6: x-y)	1.52*
784	45	171		B_{3u}	T(Ca: x), T(Al: x-y), D(AlO_6: x-y)	1.52*
785	46	176		A_u	T(Ca: z), T(Al: z), D(AlO_6: z)	2.07*
786	47	209		B_{1u}	T(Ca: z), T(Al: z)	0.85*
787	48	209		B_{3u}	T(Al: x-y), D(AlO_6: x-y), T(Ca: x-y)	1.42*
788	49	221		A_u	T(Ca: z), T(Al: z), D(AlO_6: z)	1.32*
789	50	235		B_{1u}	T(Al: z), T(Ca: z), D(AlO_6: z)	1.32*
790	51	248		B_{2u}	T(Al: x-y), T(Ca: y), D(AlO_6: x-y)	1.42*
791	52	274		B_{3u}	T(Al: x), T(Ca: x), D(AlO_6: x)	1.78*
792	53	300		B_{2u}	T(Ca: x) , T(Al: x-y), D(AlO_6: x-y)	1.06*
793	54	324		B_{2u}	T(Al: x-y), D(AlO_6: x-y), T(Ca: x-y)	1.78*
794	55	338		B_{3u}	T(Ca: y), T(Al: x), D(AlO_6: y)	0.76*
795	56	364		B_{2u}	D(AlO_6: x-y), T(Al: x), T(Ca: y)	1.32*
796	57	380		B_{3u}	D(AlO_6: x-y), T(Al: x-y), T(Ca: x)	1.32*
797	58	389		B_{1u}	D(AlO_6: z)	1.81*
798	59	389		B_{2u}	D(AlO_6: x-y), T(Ca: x-y),T(Al: x)	1.32*
799	60	392		A_u	D(AlO_6: z)	1.81*
800	61	399		B_{3u}	D(AlO_6: x-y), T(Al: x-y), T(Ca: y)	1.32*
801	62	417		B_{1u}	D(AlO_6: z)	1.81*
802	63	425		A_u	D(AlO_6: z), T(Al: z)	1.30*
803	64	435		A_u	D(AlO_6: z)	1.31*
804	65	441		B_{2u}	T(Al: x-y), D(AlO_6: x-y)	1.32*
805	66	443		B_{1u}	D(AlO_6: z)	1.31*
806	67	444		B_{3u}	T(Al: x-y), D(AlO_6: x-y)	1.32*
807	68	468		B_{3u}	T(Al: x-y), D(AlO_6: x-y)	1.32*
808	69	492		A_u	D(AlO_6: z), T(Al: z)	1.30*
809	70	494		B_{1u}	D(AlO_6: z), T(Al: z)	1.30*
810	71	502		B_{2u}	D(AlO_6: x-y), T(Al: x-y)	1.30*
811	72	510		B_{2u}	D(AlO_6: x-y)	1.13*
812	73	513		B_{3u}	D(AlO_6: x-y), T(Al: x-y)	1.13*

74	565	B_{2u}	D(AlO_6: x-y), T(Al: x-y)	1.13*
75	567	B_{3u}	D(AlO_6: x-y), T(Al: x-y)	1.13*
76	678	B_{2u}	D(AlO_6: x)	0.88*
77	681	B_{3u}	D(AlO_6: x-y), T(Al: y)	0.88*
78	701	B_{3u}	D(AlO_6: x-y), T(Al: y)	0.88*
79	722	B_{2u}	D(AlO_6: x-y), T(Al: x)	1.01*
80	772	B_{2u}	D(AlO_6: x-y), T(Al: y)	0.92*
81	800	B_{3u}	D(AlO_6: x), T(Al: x)	0.92*
82	0	B_{2u}	T(Ca, Al, O: x), acoustic mode	
83	0	B_{3u}	T(Ca, Al, O: y), acoustic mode	
84	0	B_{1u}	T(Ca, Al, O: z), acoustic mode	

Symmetries are of space group *Pbnm*.

T: translation; D: deformation.

The x, y and z, which are identical to crystal axes *a*, *b*, *c* of the calcium ferrite structure with the space group *Pbnm*, respectively, show the direction of atomic displacements.

* Values were estimated by assuming that modes with similar atomic motions have the same mode Grüneisen parameter.

Table 5. Vibrational density of states models and physical properties used for heat capacity calculations

	$MgAl_2O_4$ CF			$CaAl_2O_4$ CF		
	Lower limit (cm^{-1})	Upper limit (cm^{-1})	Number of modes	Lower limit (cm^{-1})	Upper limit (cm^{-1})	Number of modes
TA1	0	116[a]	1	0	84[a]	1
TA2	0	159[a]	1	0	116[a]	1
LA	0	225[a]	1	0	188[a]	1
OC1	140	860	81	160	580	62
OC2	–	–	–	610	800	19
V_{298} (cm^3/mol)		36.136[b]			39.765[c]	
$K_{0,298}$ (GPa)		205[d]			183[e]	
$(\partial K_{0T}/\partial T)_P$ (GPa/K)		−0.030[d]			−0.030[f]	
γ_{th}		1.50[c]			1.31[c]	

TA: transverse acoustic mode; LA: longitudinal acoustic mode; OC: optic continuum.

[a] Estimated value by Kojitani et al. (2003).

[b] Kojitani et al. (2007).

[c] This study.

[d] Sueda et al. (2009).

[e] Estimated from K_T–V relation. See text.

[f] Assumed to be the same as that of $MgAl_2O_4$ CF.

Table 6. Calculated heat capacities of calcium ferrite-type $MgAl_2O_4$ and $CaAl_2O_4$

T(K)	This study		Kojitani et al. (2003)	
	C_V (J/mol K)	C_P (J/mol K) †	C_V (J/mol K)	C_P (J/mol K)
$MgAl_2O_4$ CF				
50	5.8	5.8(4)	4.4	4.9
100	28.3	28.3(8)	26.0	26.9
200	77.2	77.6(10)	76.8	78.6
300	112.3	113.4(8)	111.8	114.6
400	133.3	135.5(6)	132.6	136.4
500	145.8	149.1(5)	145.1	149.9
600	153.6	158.0(5)	152.9	158.8
700	158.7	164.3(5)	158.1	165.1
800	162.2	168.9(5)	161.6	169.8
1000	166.4	175.6(7)	166.0	176.5
1200	168.9	180.5(9)	168.5	181.5
1400	170.3	184.5(11)	170.1	185.6
1600	171.3	188.2(13)	171.2	189.5
1800	172.0	191.6(15)	171.9	193.1
2000	172.5	195.1(18)	172.4	196.7
$CaAl_2O_4$ CF				
50	6.4	6.4(3)	6.2	6.7
100	32.0	32.0(10)	28.4	29.3
200	87.0	87.3(11)	77.6	79.4
300	121.3	122.3(8)	111.6	114.4
400	140.2	142.1(6)	132.1	135.9
500	151.0	153.7(5)	144.5	149.4
600	157.5	161.2(4)	152.5	158.4
700	161.7	166.3(4)	157.7	164.7
800	164.6	170.1(5)	161.3	169.4
1000	168.1	175.4(6)	165.8	176.3
1200	170.0	179.3(7)	168.4	181.3
1400	171.2	182.6(9)	170.0	185.5
1600	172.0	185.6(12)	171.1	189.4
1800	172.5	188.5(14)	171.8	193.0
2000	172.9	191.4(17)	172.3	196.6

†The numbers in parentheses are uncertainties.

Values for C_V and C_P by Kojitani et al. (2003) were recalculated based on their vibrational density of states model.

907 Table 7. Polynomial expressions for calculated thermal expansivities of calcium
908 ferrite-type $MgAl_2O_4$ and $CaAl_2O_4$

909 Material	$\alpha(T) = a + bT + cT^{-1} + dT^{-2}$			
910	$a\times10^5$	$b\times10^9$	$c\times10^3$	d
911 $MgAl_2O_4$ CF	2.9385	7.1252	1.1742	−1.1962
912 $CaAl_2O_4$ CF	2.2200	8.6615	3.8020	−1.4656

913 T in K and α in K^{-1}. Valid temperature range is from 290 to 2500 K.
914
915
916
917
918
919
920 Table 8. Equations of isobaric heat capacity for calcium ferrite-type $MgAl_2O_4$ and
921 $CaAl_2O_4$

922 Material	$C_P(T) = a + bT + cT^{-2} + dT^{-0.5} + eT^2$				
923	a	$b\times10^2$	$c\times10^{-6}$	$d\times10^{-3}$	$e\times10^6$
924 $MgAl_2O_4$ CF	253.62	−1.9452	−1.8422	−1.9908	6.3103
925 $CaAl_2O_4$ CF	234.01	−1.5404	−2.0893	−1.4668	5.3582

926 T in K and C_P in J/mol K. Valid temperature range is from 290 to 2500 K.
927 The heat capacity coefficients were obtained by the least squares fitting to the
928 calculated C_P data.
929
930
931

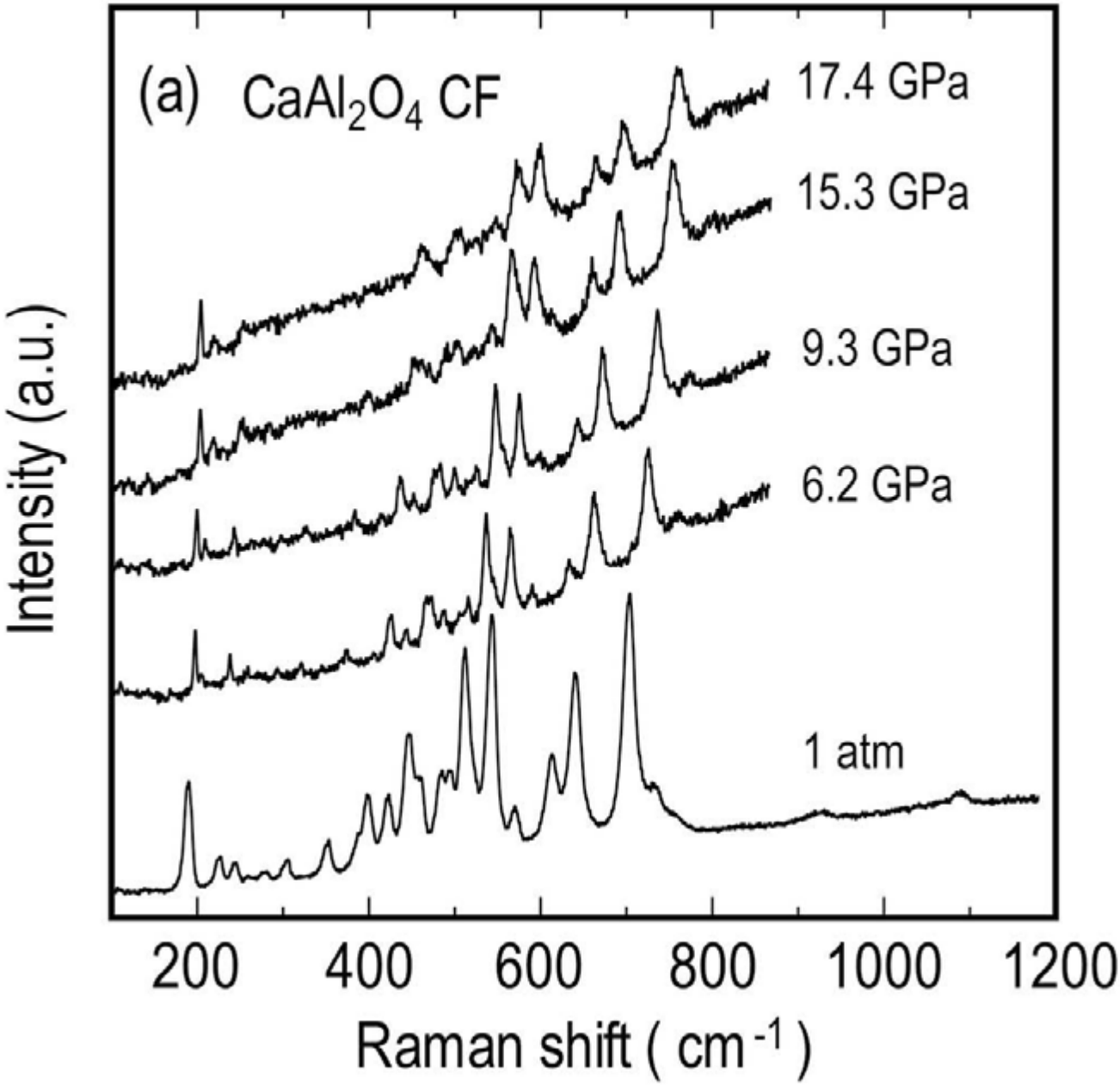
(a) $CaAl_2O_4$ CF
17.4 GPa
15.3 GPa
9.3 GPa
6.2 GPa
1 atm
Intensity (a.u.)
200
400
600
800
1000
1200
Raman shift (cm^{-1})

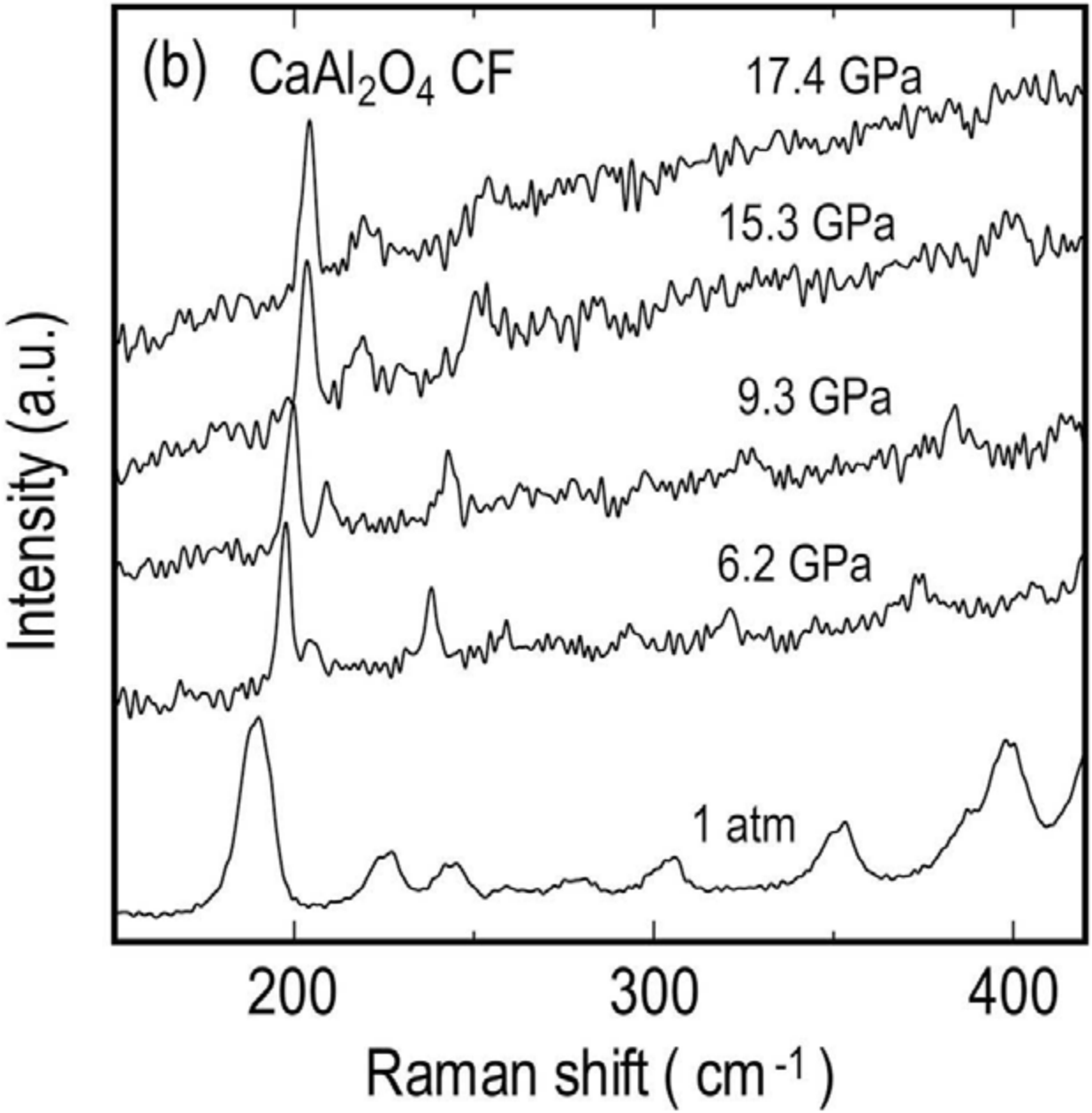
(b) $CaAl_2O_4$ CF
17.4 GPa
15.3 GPa
9.3 GPa
6.2 GPa
1 atm
Intensity (a.u.)
200
300
400
Raman shift (cm^{-1})

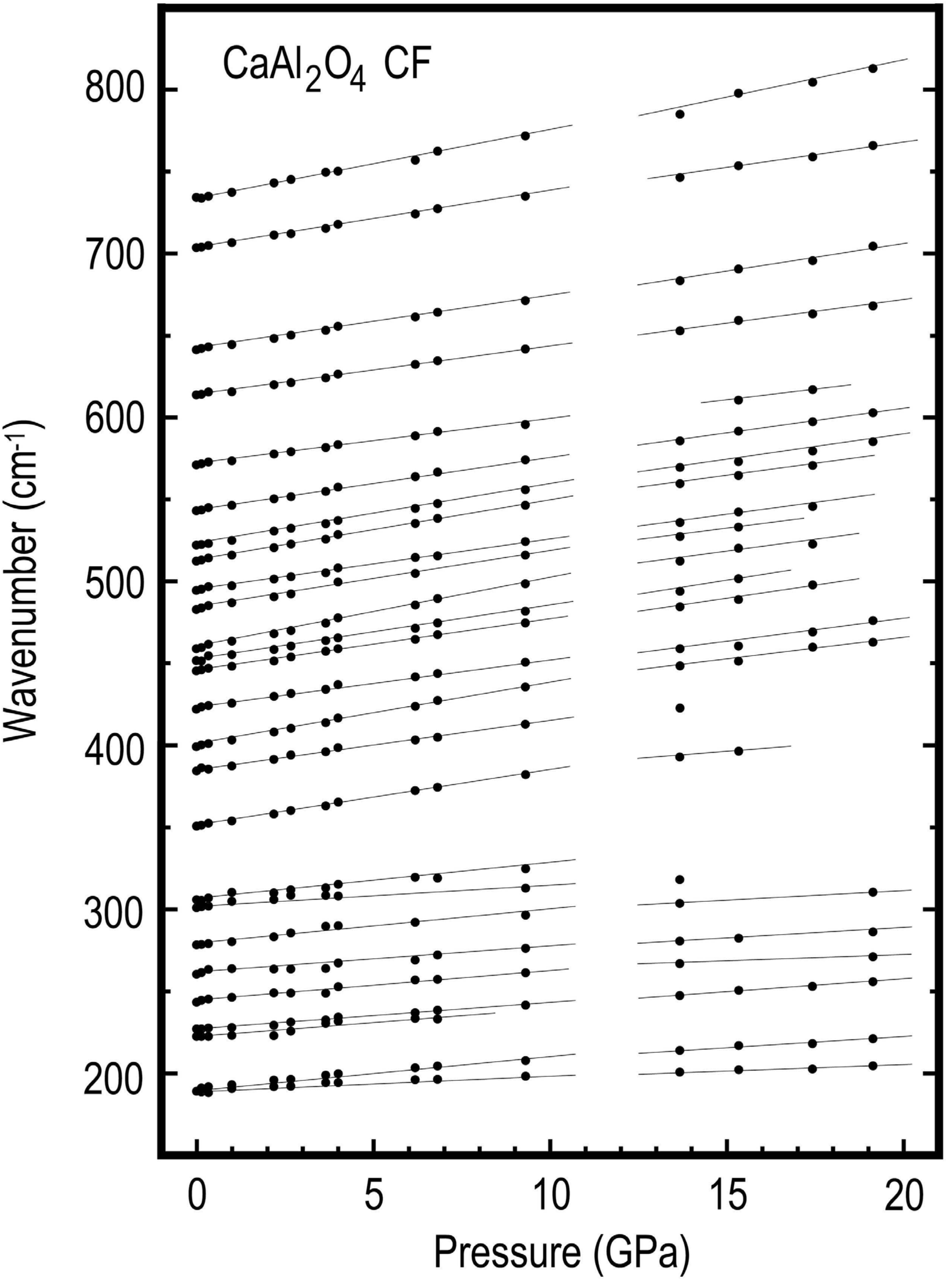
$CaAl_2O_4$ CF
800
700
600
500
400
300
200
Wavenumber (cm-1)
0
5
10
15
20
Pressure (GPa)

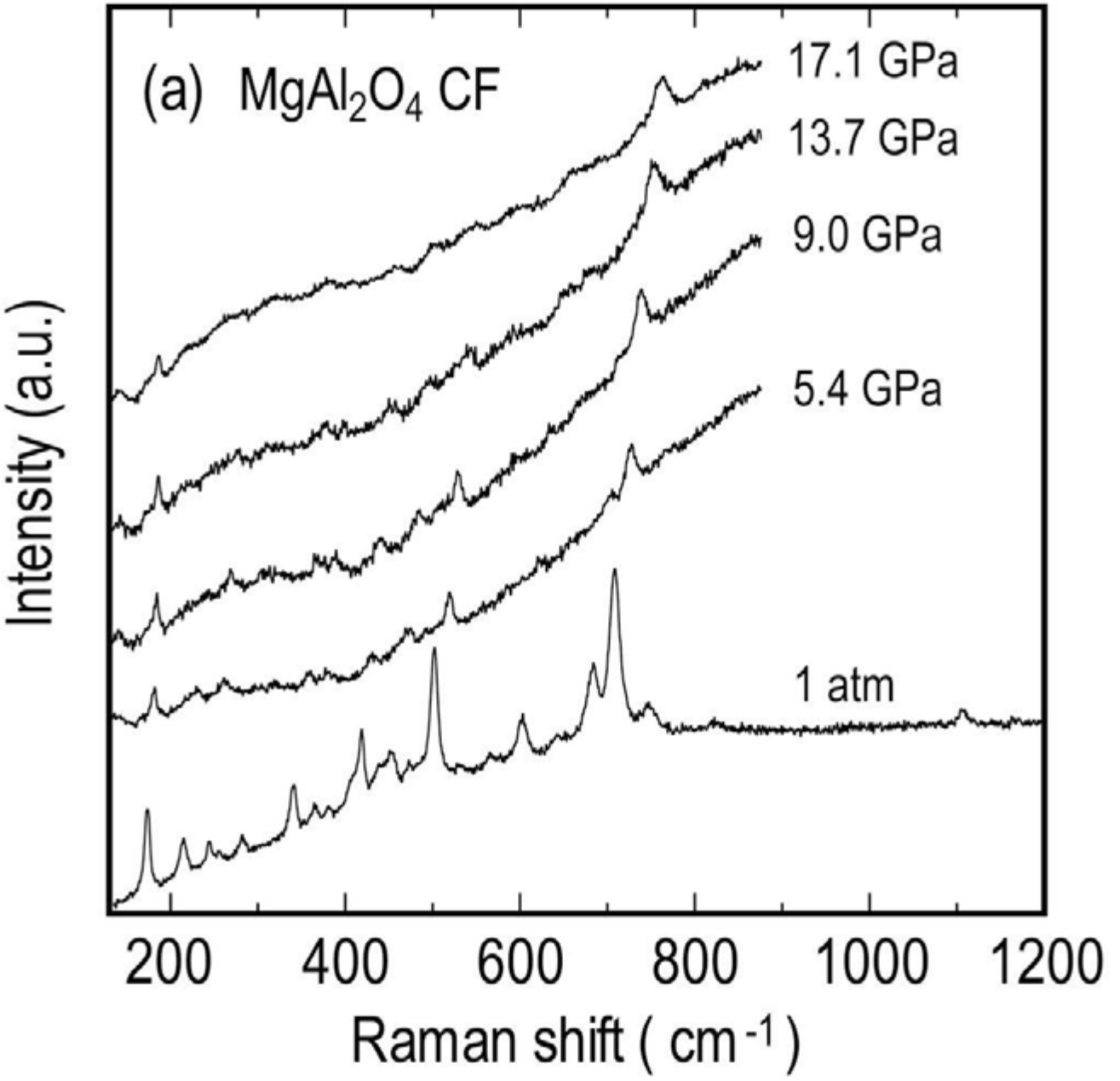
(a) MgAl2O4 CF
17.1 GPa
13.7 GPa
9.0 GPa
5.4 GPa
1 atm
Intensity (a.u.)
200
400
600
800
1000
1200
Raman shift (cm-1)

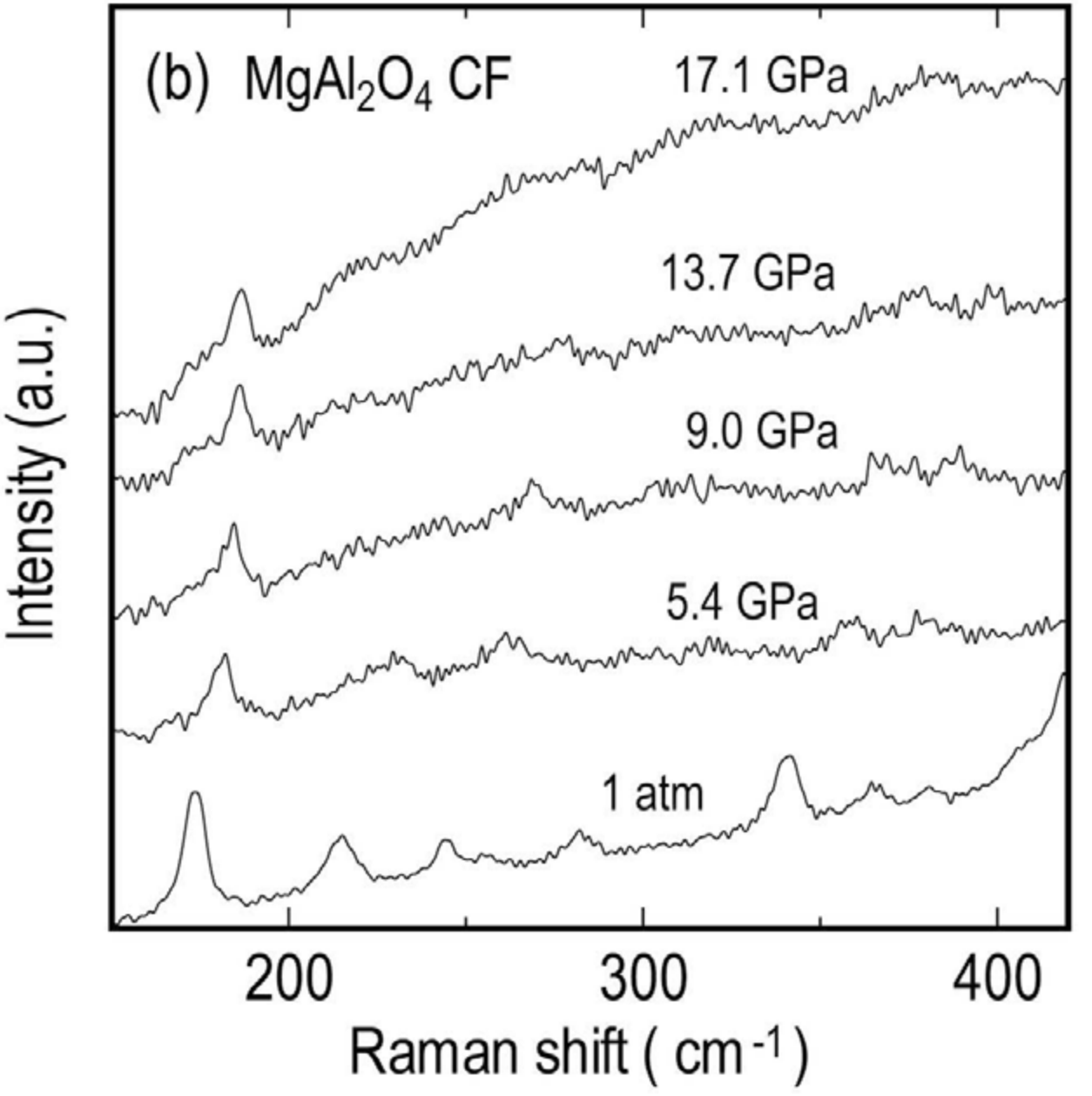
(b) $MgAl_2O_4$ CF
17.1 GPa
13.7 GPa
9.0 GPa
5.4 GPa
1 atm
Intensity (a.u.)
200
300
400
Raman shift (cm^{-1})

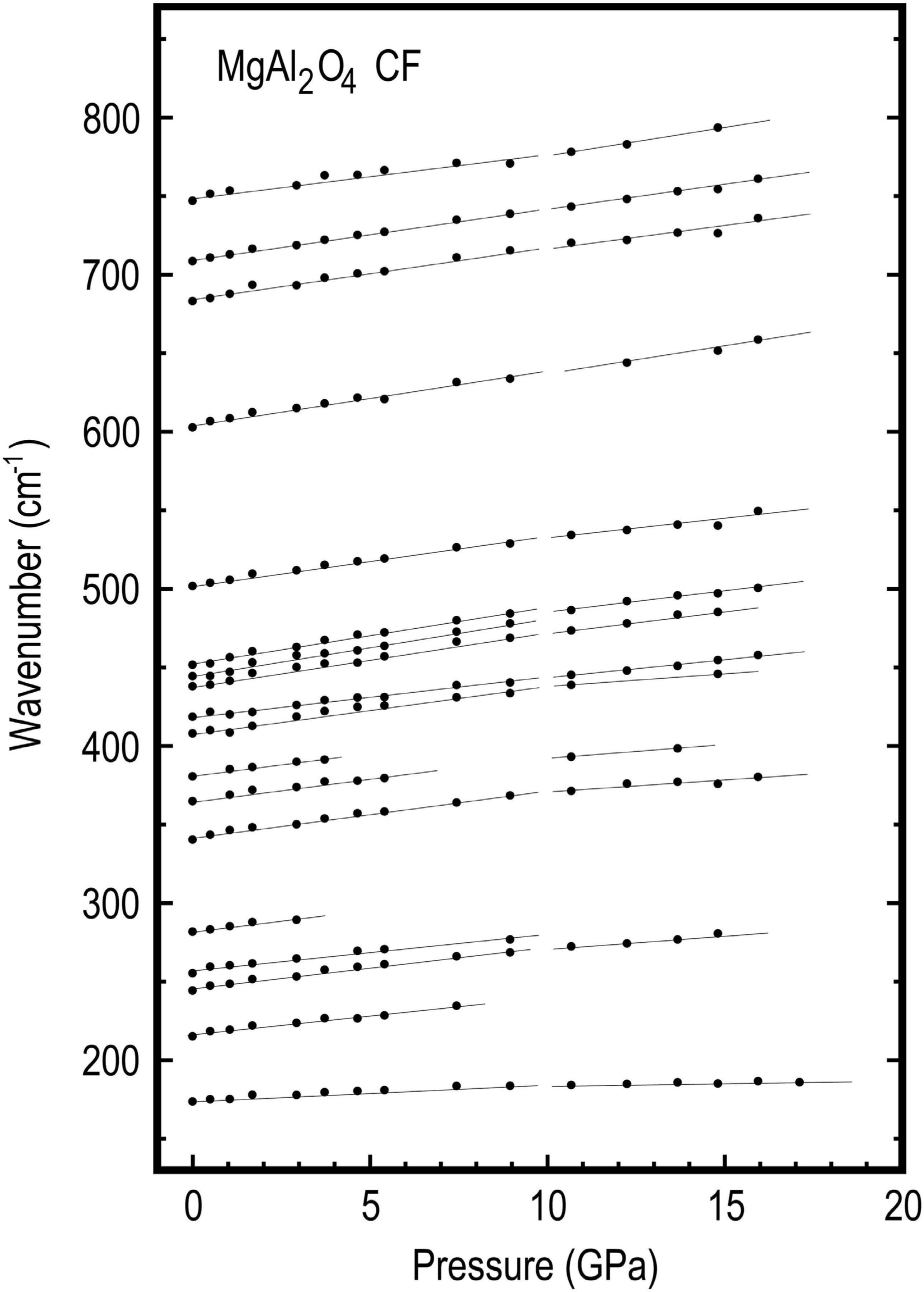
MgAl2O4 CF
800
700
600
500
400
300
200
Wavenumber (cm-1)
0
5
10
15
20
Pressure (GPa)

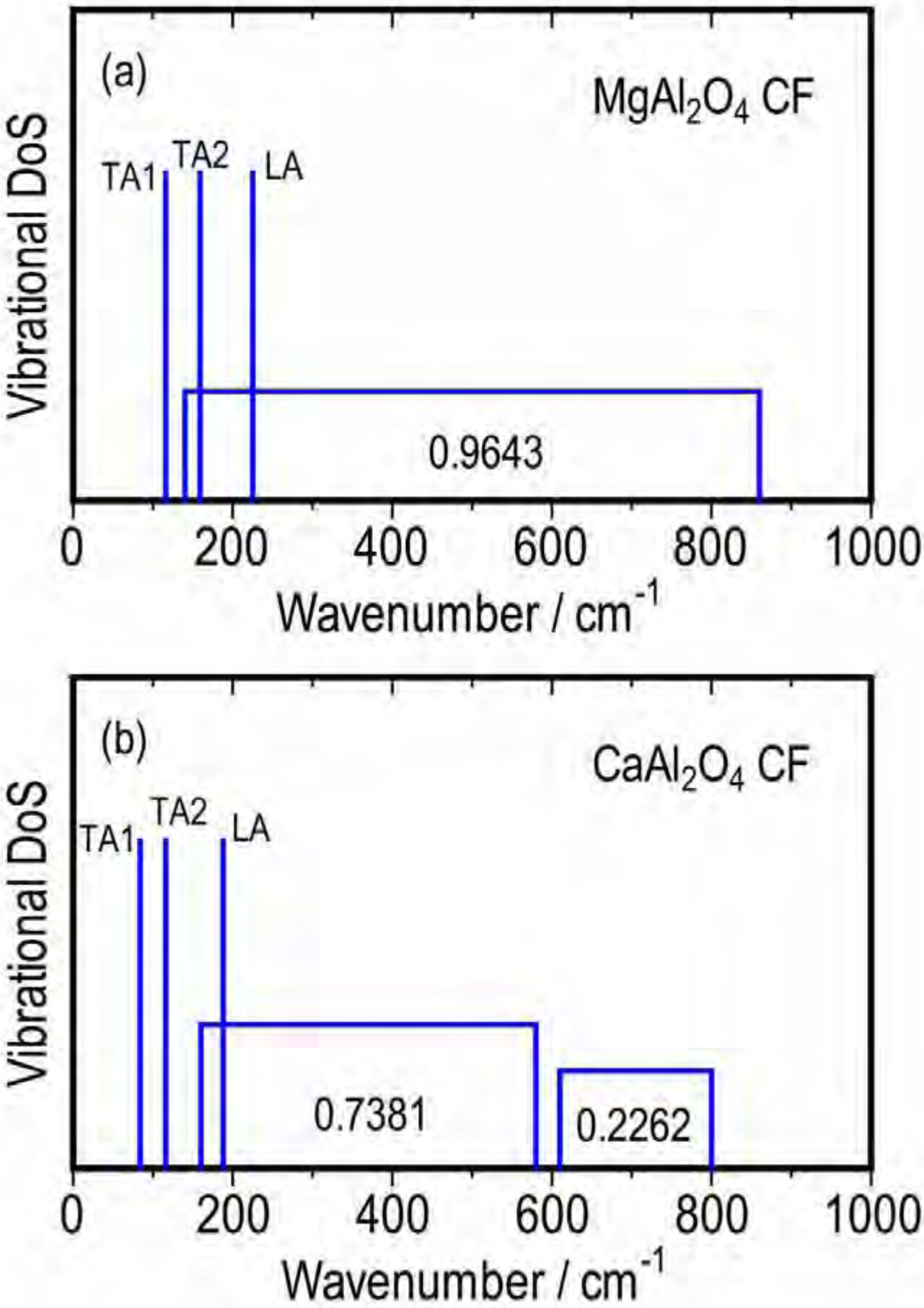
(a)
$MgAl_2O_4$ CF
TA1
TA2
LA
0.9643
Vibrational DoS
0
200
400
600
800
1000
Wavenumber / cm^{-1}
(b)
$CaAl_2O_4$ CF
TA1
TA2
LA
0.7381
0.2262
Vibrational DoS
0
200
400
600
800
1000
Wavenumber / cm^{-1}

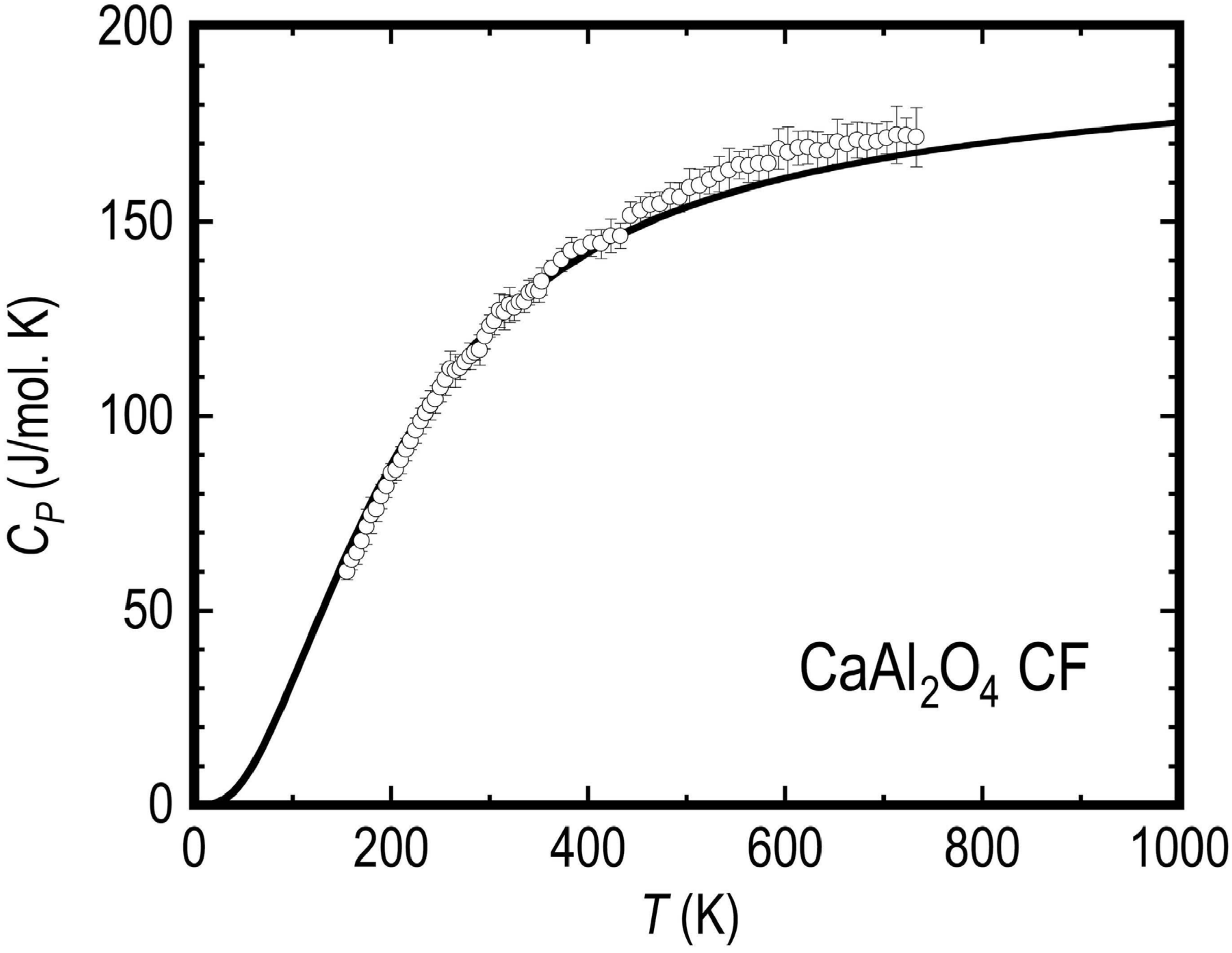
200
150
100
50
0
C_P (J/mol. K)
0
200
400
600
800
1000
T (K)
$CaAl_2O_4$ CF